

Article

A Near-Infrared BODIPY-Based Rhomboidal Metallacycle for Imaging-Guided Photothermal Therapy

Jinjin Zhang ^{1,†}, Jialin Yu ^{1,†}, Wen Li ¹, Yiqi Fan ¹, Yang Li ¹ , Yan Sun ², Shouchun Yin ^{1,*}  and Peter J. Stang ^{2,*}

¹ College of Material, Chemistry and Chemical Engineering, Key Laboratory of Organosilicon Chemistry and Material Technology, Ministry of Education, Key Laboratory of Organosilicon Material Technology, Hangzhou Normal University, Hangzhou 310036, China; zhangjinjin@stu.hznu.edu.cn (J.Z.); yujialin1@stu.hznu.edu.cn (J.Y.); 2020111009028@stu.hznu.edu.cn (W.L.); fanyiqi@stu.hznu.edu.cn (Y.F.); liyang@hznu.edu.cn (Y.L.)

² Department of Chemistry, University of Utah, 315 South 1400 East, Room 2020, Salt Lake City, UT 84112, USA; elaine.sun@utah.edu

* Correspondence: yinsc@hznu.edu.cn (S.Y.); stang@chem.utah.edu (P.J.S.)

† These authors contributed equally to this work.

Abstract: Although boron dipyrromethene (BODIPY)-based metallacycles are expected to be promising candidates for imaging probes and therapeutic agents, their biomedical applications are restricted by their short absorption/emission wavelengths. In this work, we report a rhombic metallacycle **M** with broad absorption in the near-infrared (NIR) range and emissions at wavelengths >800 nm, which exhibits an efficient photothermal conversion capacity. Metallacycle **M** was encapsulated via Pluronic F127 to fit the biotic environment, resulting in the generation of F127/**M** nanoparticles (NPs) with high hydrophilicity and biocompatibility. *In vitro* studies demonstrated that the F127/**M** NPs underwent efficient cellular uptake and exhibited satisfactory photothermal therapeutic activity. Furthermore, *in vivo* experiments revealed that tumor growth was effectively inhibited, and the degree of undesirable biological damage was minimal in treatment with F127/**M** NPs and laser irradiation. Finally, the F127/**M** NPs could be visualized through NIR fluorescence imaging in living mice, thereby allowing their distribution to be monitored in order to enhance treatment accuracy during photothermal therapy. We envision that such BODIPY-based metallacycles will provide emerging opportunities for the development of novel therapeutic agents for biomedical applications.

Keywords: metallacycle; boron dipyrromethene; photothermal therapy



Citation: Zhang, J.; Yu, J.; Li, W.; Fan, Y.; Li, Y.; Sun, Y.; Yin, S.; Stang, P.J. A Near-Infrared BODIPY-Based Rhomboidal Metallacycle for Imaging-Guided Photothermal Therapy. *Inorganics* **2022**, *10*, 80. <https://doi.org/10.3390/inorganics10060080>

Academic Editors: Rainer Winter and Bruno Therrien

Received: 23 May 2022

Accepted: 10 June 2022

Published: 13 June 2022

Publisher's Note: MDPI stays neutral with regard to jurisdictional claims in published maps and institutional affiliations.



Copyright: © 2022 by the authors. Licensee MDPI, Basel, Switzerland. This article is an open access article distributed under the terms and conditions of the Creative Commons Attribution (CC BY) license (<https://creativecommons.org/licenses/by/4.0/>).

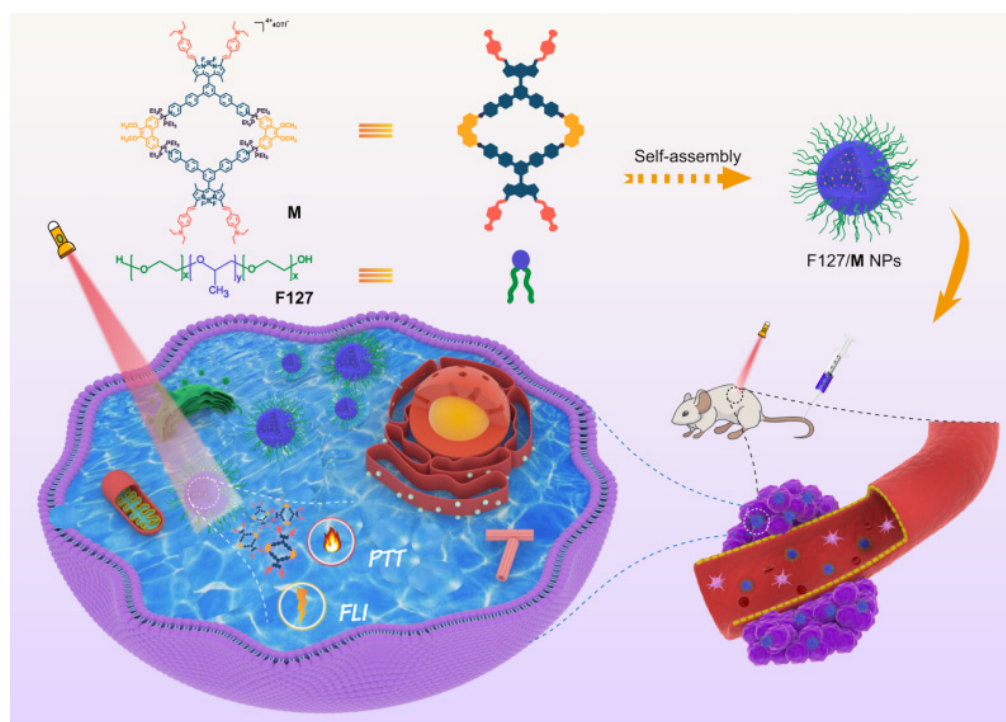
1. Introduction

Coordination-driven self-assembly provides a feasible and effective strategy for obtaining metal-organic macrocycles (MOCs) with well-defined morphologies and sizes based on the metal–ligand bonds present between the organic donors and the metal acceptors [1–5]. On account of the diverse metal centers and ligands available for their construction, MOCs can be easily constructed from the bottom up [6–9], and they can serve as integrated function platforms for extensive applications (e.g., optical materials [10–12], chemical sensors [13–15], catalysis [16,17], bioimaging [18,19], and biotherapy [20,21]) via pre- and post-self-assembly functional modifications. For example, fluorescent metallacycles with anticancer potential have attracted widespread interest in medicinal chemistry, not only because of the adjustable bioactivity of the metal centers and organic ligands, but also due to the fact that they can be visually localized *in vivo* [22]. Thus, the judicious selection of organic donors and metal acceptors plays an essential role in achieving superior fluorescent metallacycles for theranostics [23,24].

As an extensively investigated organic chromophore, boron dipyrromethene (BODIPY) is of particular interest because of its excellent properties, such as its facile synthesis and structural diversification, its high absorption coefficients and fluorescence quantum

yields, its high photostability, and its excellent chemical stability [25–31]. Owing to these advantages, BODIPYs have been widely applied in photovoltaic devices [32–35], fluorescent probes [36–39], bioimaging [40–42], photodynamic therapy (PDT) [43–46], and photothermal therapy (PTT) [47–50]. It has been demonstrated that integrating BODIPYs as building blocks into metallacycles may result in a range of advantages [22]. More specifically, when well-defined metallacycles are employed, BODIPY units can endow the metallacycles with fluorescent characteristics and bioactivity, and the photophysical properties of the formed BODIPY-based metallacycles can be modulated by directional transition dipole moments or efficient energy transfer. Based on these factors, a number of efforts were made to develop BODIPY-based metallacycles for bioapplications [23,51–53]. For example, Huang et al. [54] reported two high-emission platinum(II)-centered metallacycles containing BODIPY-derived ligands, which were suitable for fluorescence imaging-guided chemo-photodynamic synergistic therapy upon light irradiation at 400–700 nm. However, strong absorption in the near-infrared (NIR) region (650–1700 nm) is desirable to allow deeper penetration and produce minimal biological damage within healthy tissue. To date, very few BODIPY-based metallacycles have been reported that exhibit intense NIR absorption [51].

Herein, we describe an NIR-absorbing and emissive metallacycle **M** constructed via coordination-driven self-assembly using 120° dipyrindyl BODIPY ligand **1** and 60° phenanthrene-based diplatinum(II) **2** as the building blocks (Scheme 1). Based on a Knoevenagel condensation, a *N,N*-diethyl-4-aminophenyl group was introduced into the 3,5-positions of the BODIPY cores to obtain BODIPY ligands with strong NIR absorption properties. Due to its NIR emission, the visualization and localization of metallacycle **M** were also investigated. Furthermore, metallacycle **M** was encapsulated in micelles of Pluronic F127 to produce F127/**M** nanoparticles (NPs), whose photothermal conversion behaviors and fluorescent imaging properties were evaluated both *in vitro* and *in vivo*. The tumor growth inhibition ability of the F127/**M** NPs was also examined to determine the potential for MOCs to act as versatile platforms for theranostics.



Scheme 1. Preparation of the F127/**M** NPs from metallacycle **M** and F127, and a schematic illustration of their application in imaging-guided photothermal therapy.

2. Results and Discussion

2.1. Synthesis of Metallacycle **M**

As outlined in Scheme S1, BODIPY ligand **1** was initially synthesized via a Knoevenagel condensation reaction and a following palladium-catalyzed coupling reaction. Subsequently, the coordination-driven self-assembly of BODIPY-based 120° dipyriddy donor **1** with phenanthrene-based 60° diplatinum(II) acceptor **2** produced rhomboidal Pt(II) metallacycle **M** in an excellent yield (>90%). The metallacycle was then characterized using multinuclear NMR spectroscopy (i.e., ^1H and $^{31}\text{P}\{^1\text{H}\}$) and electrospray ionization time-of-flight mass spectrometry (ESI-TOF-MS). In the $^{31}\text{P}\{^1\text{H}\}$ NMR spectrum, a sharp singlet peak was observed for **M** at 14.25 ppm, with concomitant ^{195}Pt satellite peaks also being present ($J_{\text{Pt-P}} = 2674.3$ Hz), thereby indicating a single phosphorus environment. In addition, an upfield shift by 7.33 ppm in comparison with the corresponding signal of acceptor **2** confirmed the formation of metal–ligand bonds (Figure 1a,b). As shown in the ^1H NMR spectrum of **M** (Figure 1c–e), downfield shifts were observed for the α -pyridyl H_a protons (i.e., from 8.65 to 8.68 ppm) and for the β -pyridyl H_b proton (i.e., from 7.81 to 7.93 ppm), compared to the corresponding shifts of the free BODIPY-based dipyriddy ligand **1**; these shifts were attributed to the reduced electron densities caused by coordination with the metal. In addition, aromatic protons H_c , H_d , H_e , and H_f of ligand **1** and aromatic protons H_1 , H_2 , and H_3 of Pt(II) acceptor **2** shifted upfield. ESI-TOF-MS provided further evidence of the formation of **M**, wherein isotopically resolved peaks were observed at m/z values of 1414.945 and 1023.905, which corresponded to $[\text{M}-3\text{OTf}]^{3+}$ and $[\text{M}-4\text{OTf}]^{4+}$, respectively (Figures 1g and S17).

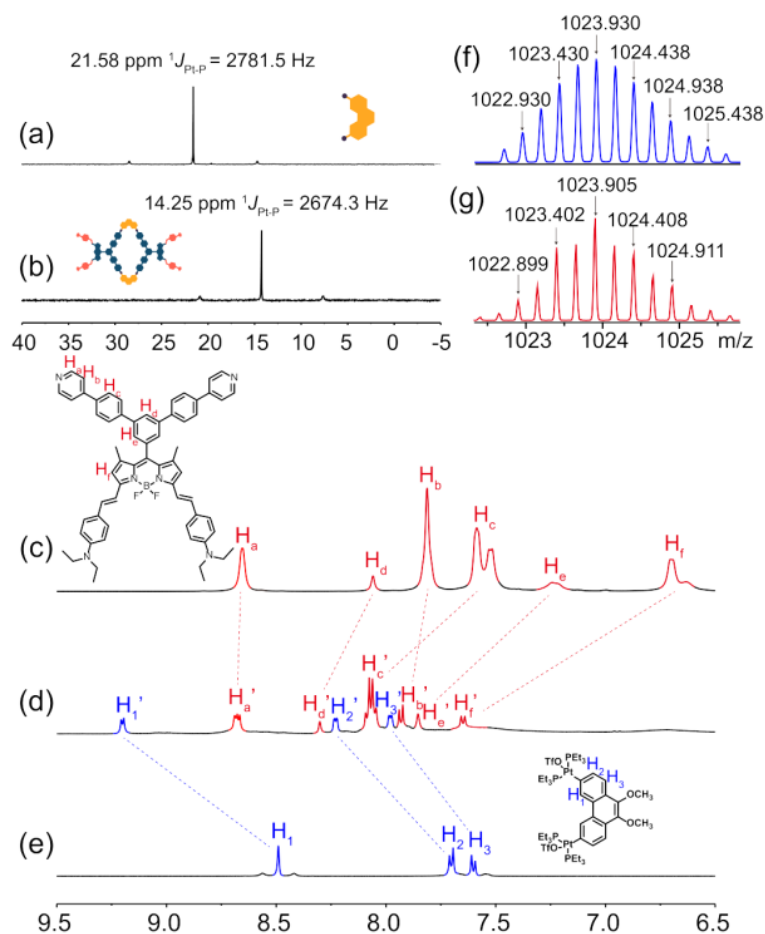


Figure 1. $^{31}\text{P}\{^1\text{H}\}$ NMR spectra of (a) **2** and (b) **M** (202 MHz, CD_3OD , 298 K). Partial ^1H NMR spectra of (c) ligand **1**, (d) metallacycle **M**, and (e) acceptor **2** (500 MHz, CD_2Cl_2 , 298 K). (f) Calculated (blue) and (g) experimental (red) ESI-TOF-MS peaks of $[\text{M}-4\text{OTf}]^{4+}$.

2.2. Fabrication and Characterization of F127/M NPs

Owing to the hydrophobicity of **M**, we introduced F127 for encapsulation via the precipitation method to yield F127/M NPs with enhanced solubility, biocompatibility, and tumor accumulation properties. As depicted in Figure 2a,b, transmission electron microscopy (TEM) and dynamic light scattering (DLS) were used to confirm the morphology and size of the NPs, and both techniques indicated a uniform size of ~ 150 nm, thereby indicating their potential for accumulating in tumor tissues owing to the enhanced permeability and retention (EPR) effect [55]. Furthermore, after three weeks in storage, it was found that the NP size remained relatively constant, thereby demonstrating their excellent colloidal stability (Figure 2b). The F127/M NPs displayed broad absorption in the NIR range from 600 to 900 nm, with a maximum absorption peak being observed at 747 nm in an aqueous solution; this represented a more pronounced red shift compared to that observed in acetone (i.e., 716 nm). Based on the UV-vis absorption spectrum of **M**, the **M**-loading efficiency of the F127/M NPs was calculated as 10% (Figure S20). In addition, the maximum emission peak of the F127/M NPs was 820 nm in the NIR-I window (Figure 2c) and the fluorescent quantum yield was 0.31%.

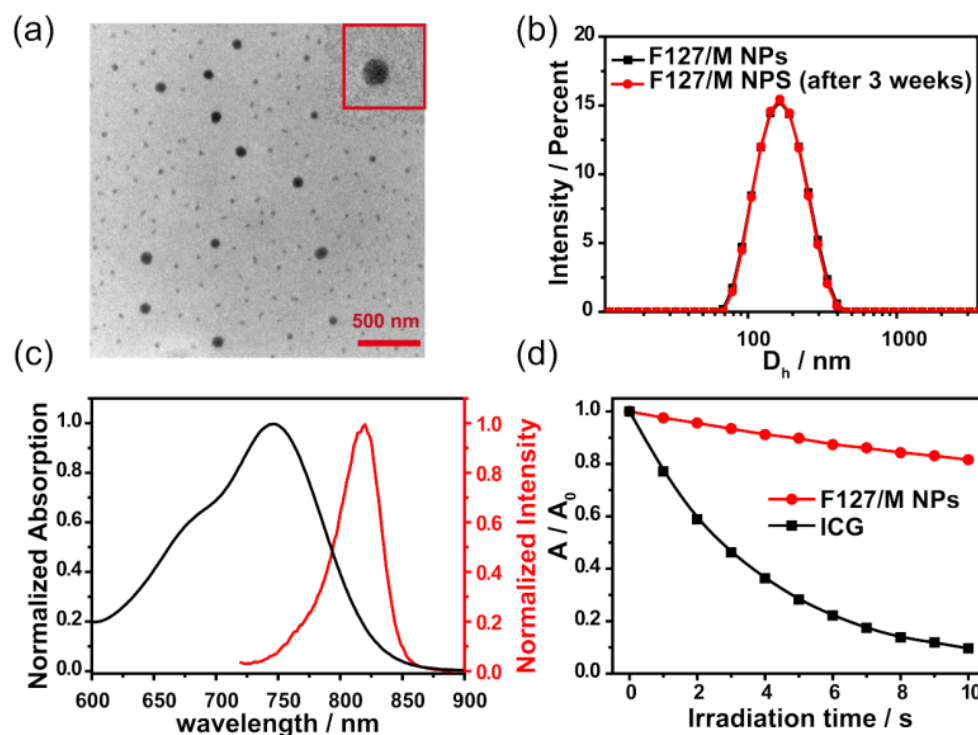


Figure 2. (a) TEM image and (b) DLS results for F127/M NPs immediately after preparation and after three weeks of storage. (c) Normalized UV-vis absorption and fluorescence spectra of the NPs in water ($\lambda_{ex} = 660$ nm). (d) Relative absorption changes recorded for aqueous solutions of F127/M NPs or ICG at 745 or 779 nm, respectively, over different irradiation times (660 nm, 1.0 W/cm^2).

The colloidal stability of **M** is an important property of phototherapeutic agents for applications *in vivo*, which was measured by **M** treatment with irradiation. Insignificant changes in $^{31}\text{P}\{^1\text{H}\}$ NMR spectra of **M** were detected after irradiation for 10 min (Figure S20), indicating the structural stability of **M**. Furthermore, from comparison between the relative absorbance changes in F127/M NPs and ICG in aqueous media upon irradiation, F127/M NPs exhibited better photobleaching resistance, aiding in the maintenance of the phototherapy effect (Figures 2d and S21).

2.3. Photothermal Properties of F127/M NPs

Subsequently, we systematically evaluated the photothermal properties of the F127/M NPs under 660 nm laser exposure. As shown in Figure 3a–c, upon 660 nm laser irradiation

for 10 min, the temperature of the F127/M NP solution elevated in a concentration- and power-density-dependent manner. With an increase in F127/M NP concentration (from 0 to 20 μM), the temperature of the F127/M NP solution eventually rose by 4.3 to 43 $^{\circ}\text{C}$, and it was 8.4 to 63.9 $^{\circ}\text{C}$ warmer upon increasing power density (from 0.3 to 1.8 W/cm^2), revealing efficient photothermal conversion with tunability. Based on the relevant literature [49], the photothermal conversion efficiency (PCE) of the F127/M NPs was calculated to be 36% based on the cooling process (Figure 3d). Photothermal stability is a necessary factor for photothermal agents during cancer treatment. Gratifyingly, the F127/M NPs were confirmed to possess high photothermal stability, as demonstrated by the results that the temperature elevation of the F127/M NP aqueous solution remained unaltered after five heating/cooling cycles (Figure 3e). Overall, these results indicate that the F127/M NPs possessed efficient photothermal conversion properties and high photostability, which are beneficial for their use as promising photothermal agents.

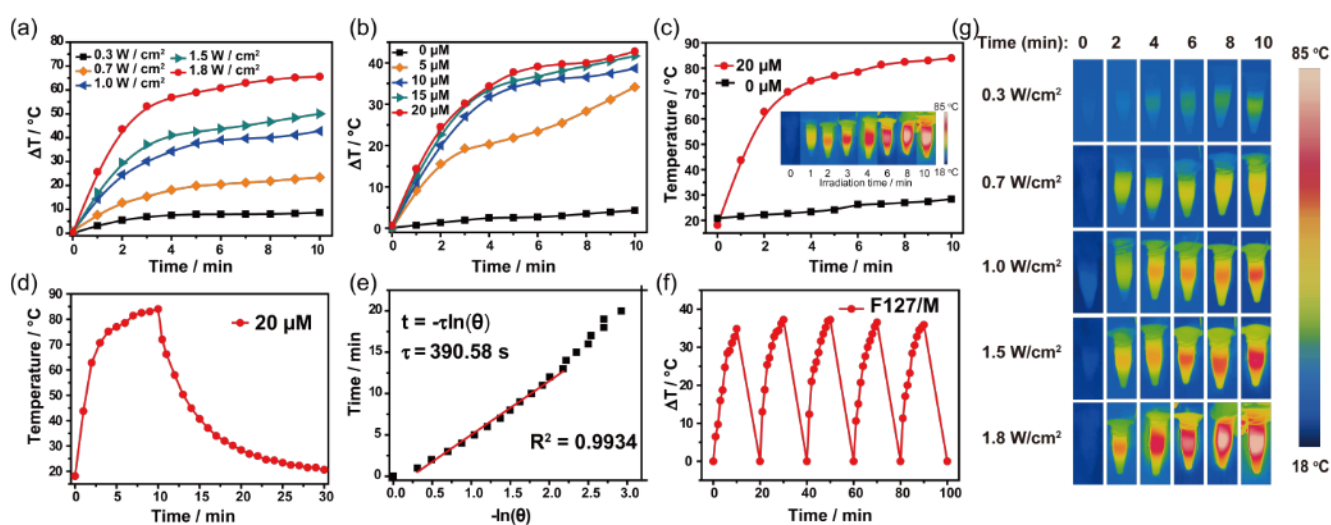


Figure 3. (a) Photothermal conversion of F127/M NPs (20 μM) under laser irradiation at different power densities (660 nm, 0.3–1.8 W/cm^2). (b) Photothermal conversion of F127/M NPs at different concentrations (5–20 μM) under laser irradiation (660 nm, 1.0 W/cm^2). (c) Photothermal conversion of F127/M NPs at different concentrations (0 and 20 μM) under laser irradiation (660 nm, 1.0 W/cm^2). Insert: IR thermal images of F127/M NPs. (d) Photothermal heating curves of F127/M NPs under irradiation (660 nm, 1.8 W/cm^2) for 10 min and subsequent natural cooling. (e) Time constants for calculation of the PCE by applying the linear time data from the cooling period to the negative natural logarithm of temperature. (f) Photothermal stability of F127/M NPs under laser irradiation (660 nm, 1.0 W/cm^2) over five heating/cooling cycles. (g) IR thermal images of F127/M NPs following irradiation at different laser power densities (660 nm, 0.3–1.8 W/cm^2).

2.4. In Vitro Photonic Cytotoxicity and Antitumor Therapy

To determine the *in vitro* photonic cytotoxicity of the FM127/M NPs, we initially assessed their cellular uptake via flow cytometry (FCM). As shown in Figure 4a, the group treated with F127/M NPs exhibited an extremely higher fluorescence intensity than the control group, thereby indicating that the F127/M NPs could successfully enter the cells. In addition, the quantitative mean fluorescence intensity (MFI) also intuitively verified their cellular internalization (Figure 4b). Based on these observations and the satisfactory photothermal properties of the F127/M NPs, we were encouraged to investigate their efficacy at the cytological level. Thus, the phototoxicity and dark toxicity of the F127/M NPs in U87 cancer cells were examined using an MTT assay (Figure 4c). >80% cell viability was observed, even at high concentrations of F127/M NPs in darkness, thereby indicating the good biocompatibility of the F127/M NPs. In contrast, under 660 nm laser irradiation at 1.0 W/cm^2 , the cell viability gradually decreased with an increase in F127/M NP concentration, which suggested dose-dependent cytotoxicity. To further verify the

phototherapeutic properties of the F127/M NPs, calcein-AM (green) and propidium iodide (PI, red) dyes were used to perform live–dead cell co-staining fluorescence experiments. As shown in Figure 4d, the control group (without the F127/M NPs) exhibited a uniform and bright green fluorescence even under laser irradiation, indicating that essentially no cell damage occurred under laser irradiation alone. In addition, the green fluorescence of the F127/M NP group demonstrated their stability in darkness. However, distinct red fluorescence was observed in the U87 cells treated with the F127/M NPs plus irradiation (660 nm, 1.0 W/cm²), and the area of red fluorescence increased upon increasing the NP concentration from 20 to 40 µg/mL. These results therefore confirm the strong photothermal potential of the F127/M NPs, which demonstrates their potential for use in PTT applications *in vivo*.

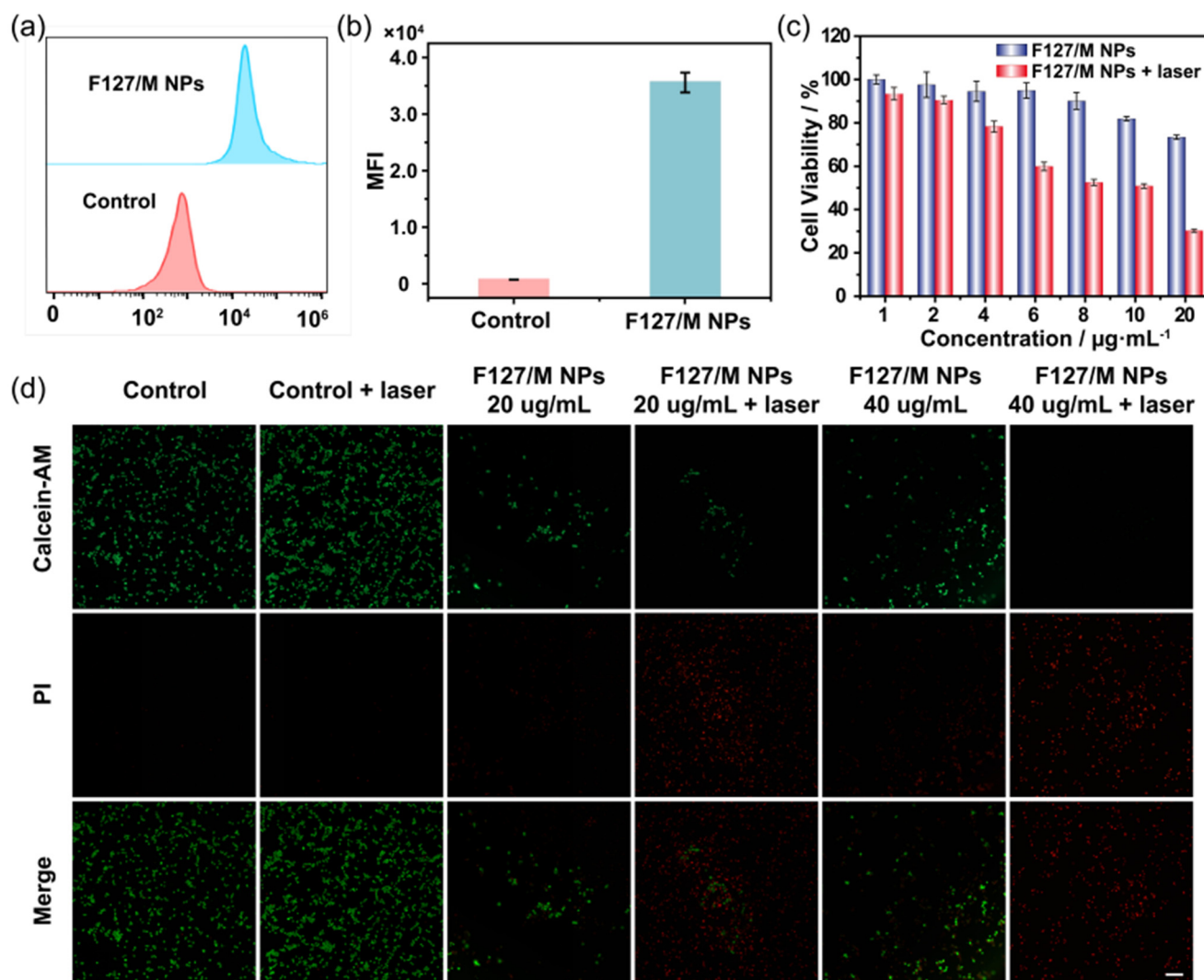


Figure 4. (a,b) Flow cytometry of U87 cells incubated with F127/M NPs. (c) Cell viability of U87 cells incubated with F127/M NPs at different concentrations in darkness and after laser irradiation (660 nm, 1.0 W/cm², 30 s). (d) Calcein-AM-/PI-containing fluorescence imaging of U87 cells after different treatments. Laser irradiation: 660 nm, 1.0 W/cm², 5 min. Scale bar: 50 µm.

2.5. *In Vivo* Imaging and Antitumor Effect

In vivo imaging is essential for both drug localization and tumor phototherapy. The intense absorption and emission provided by F127/M NPs in the NIR region indicated their strong potential for use in fluorescence imaging *in vivo*. Thus, we injected U87 tumor-bearing mice with F127/M NPs or PBS and evaluated the fluorescence images recorded over time (i.e., 1, 4, 8, 16, and 24 h). As shown in Figure 5a,b, the fluorescence signal

in the group treated with F127/M NPs gradually increased at the tumor site over time, reaching the brightest red fluorescence after 24 h. Subsequently, the effective accumulation of F127/M NPs in tumors was further verified by *ex vivo* fluorescence imaging of a tumor and of the major organs (i.e., heart, liver, spleen, lung, and kidney). As shown in Figure 5c,d, the F127/M NPs mainly accumulated in the liver and in the tumor, which was likely due to hypermetabolism in the mouse models, in addition to the EPR effect described above. These results indicate that F127/M NPs could effectively accumulate at the tumor site, and the fluorescent signal could be used to offer therapeutic guidance and enhance the *in vivo* antitumor effects of this system.

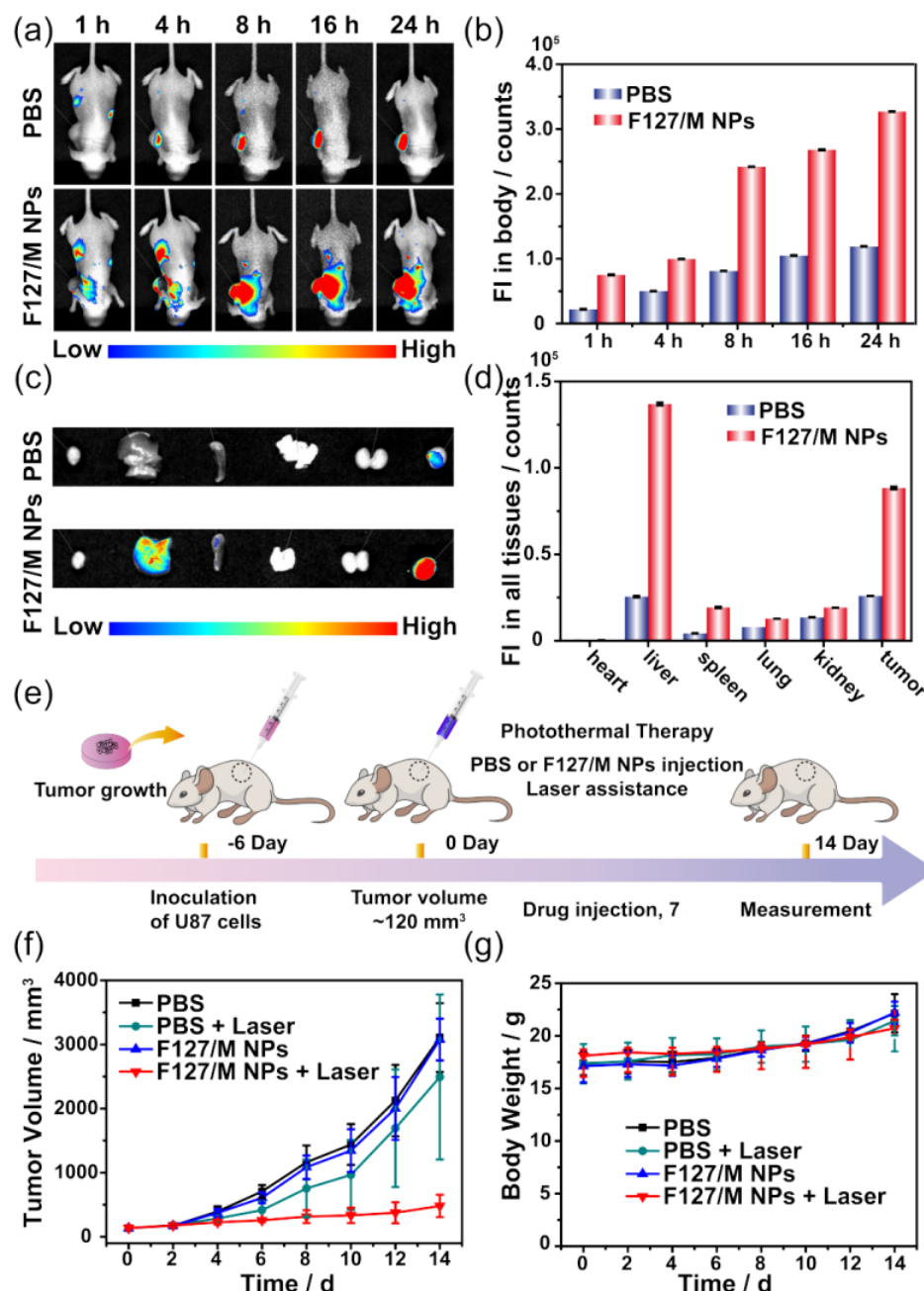


Figure 5. (a) Fluorescence images and (b) fluorescence intensities of tumor in U87 tumor-bearing mice at different time intervals (1, 4, 8, 16, and 24 h) after treatment with PBS or F127/M NPs. (c) *Ex vivo* fluorescence imaging and (d) *ex vivo* fluorescence intensities of a tumor and of the major organs (i.e., heart, liver, spleen, lung, and kidney) after treatment with PBS or F127/M NPs. (e) Schematic illustration of the *in vivo* treatment process. Changes in the (f) tumor volume and (g) body weight of the U87 tumor-bearing mice in the different treatment groups.

Encouraged by the remarkable *in vitro* anticancer activity and *in vivo* imaging results obtained for the F127/**M** NPs, we further evaluated their PTT efficiency using the U87 tumor-bearing mouse model *in vivo* (Figure 5e). PBS or F127/**M** NPs were injected intratumorally into U87 tumor-bearing mice, followed by laser irradiation treatment (660 nm, 1.0 W/cm²) at a post-administration time of 10 min. Subsequently, tumor volume and mouse body weight were recorded every 2 d for 14 d. As shown in Figure 5f, in the absence of irradiation, both PBS and F127/**M** NP groups exhibited the fastest tumor growth among the various groups, with the tumor volumes reaching ~3100 mm³. The PBS + Laser group also showed rapid tumor growth, but it was slower compared to the above two groups. This was likely due to the fact that continuous laser irradiation at 1.0 W/cm² was capable of producing a slight temperature increase, thereby inhibiting tumor growth to a certain extent. In contrast, the F127/**M** NP + Laser group demonstrated significant suppression of tumor growth in mice within the 14 d period. The photographic images recorded for the four mouse tumor groups after 14 d directly confirmed that the F127/**M** NPs could effectively inhibit tumor growth under constant laser irradiation (Figure S22). Finally, to examine the biosafety of the F127/**M** NPs, we evaluated their systemic toxicity based on the mouse body weight from U87 tumor-bearing nude mice after the different treatments. During the 14 d experimental period, the body weights of all mice gradually increased (Figure 5g), which indicates that the F127/**M** NPs could be used as biocompatible and biosafe anticancer agents for tumor therapy.

3. Conclusions

In summary, a near-infrared (NIR) boron dipyrromethene (BODIPY)-based rhomboidal metallacycle **M** was successfully formed by the coordination-driven self-assembly of strongly NIR-absorbing BODIPY ligands and phenanthrene-based Pt(II) acceptors, which not only served as diagnostic agents for bioimaging, but also could be utilized as a class of efficient photothermal reagents for photothermal therapy. In addition, following encapsulation by Pluronic F127, the F127/**M** nanoparticles (NPs) demonstrated enhanced photothermal performance with a high photothermal conversion efficiency of 36% and remarkable photobleaching resistance. *In vitro* studies showed that the F127/**M** NPs, with good biocompatibility, were successfully taken up by tumor cells, and that under laser irradiation, they selectively and efficiently damaged these cells. Moreover, the F127/**M** NPs also exhibited excellent antitumor PTT effects *in vivo*. Ultimately, this work presents a strategy for the construction of diagnostic and therapeutic agents through a BODIPY-based metallacycle, wherein the properties can be modulated by varying the individual building blocks rather than the overall design. Therefore, this work inspires insight into the development of metallacycle-based imaging-guided therapeutic agents.

Supplementary Materials: The following supporting information can be downloaded at: <https://www.mdpi.com/article/10.3390/inorganics10060080/s1>, Scheme S1: Synthetic route to **M** and chemical structures of compounds; Figure S1–S19: NMR spectra, ESI-HRMS spectra, FT-IR spectra and fluorescence spectra; Figure S20: (a) Concentration-dependent absorbance and (b) the standard curve of **M** in acetone; Figure S21: UV–vis absorption spectra and ³¹P{¹H} NMR spectra; Figure S22: Photographs of U87 tumor-bearing nude mice. [49,56,57].

Author Contributions: Conceptualization, S.Y. and P.J.S.; methodology: S.Y., P.J.S., Y.L. and Y.S.; formal analysis: J.Z., J.Y., W.L. and Y.F.; investigation, J.Z., J.Y., W.L. and Y.F.; data curation, J.Y., J.Z. and W.L.; writing—original draft preparation, J.Z. and J.Y.; writing—review and editing, S.Y., P.J.S., Y.S. and Y.L.; funding acquisition, S.Y. and Y.L. All authors have read and agreed to the published version of the manuscript.

Funding: This research was funded by the National Natural Science Foundation of China (grant numbers 21971049 and 51903070) and “Ten-thousand Talents Plan” of Zhejiang Province (grant number 2019R52040).

Institutional Review Board Statement: The mice were housed at the Laboratory Animal Center of Hangzhou Normal University with use license number SYXK (Zhejiang) 2020-0026, and cultivated in a pathogen-free environment with appropriate humidity and temperature. All animal procedures were performed in accordance with the animal care and use guidelines of the Organizational Animal Care and Use Committee.

Informed Consent Statement: Not applicable.

Data Availability Statement: Not applicable.

Conflicts of Interest: The authors declare no conflict of interest.

References

1. Zhao, J.; Zhou, Z.X.; Li, G.F.; Stang, P.J.; Yan, X.Z. Light-emitting self-assembled metallacages. *Natl. Sci. Rev.* **2021**, *8*, nwab045. [[CrossRef](#)] [[PubMed](#)]
2. Sun, Y.; Chen, C.; Stang, P.J. Soft Materials with Diverse Suprastructures via the Self-Assembly of Metal–Organic Complexes. *Acc. Chem. Res.* **2019**, *52*, 802–817. [[CrossRef](#)] [[PubMed](#)]
3. Sepehrpour, H.; Fu, W.; Sun, Y.; Stang, P.J. Biomedically Relevant Self-Assembled Metallacycles and Metallacages. *J. Am. Chem. Soc.* **2019**, *141*, 14005–14020. [[CrossRef](#)] [[PubMed](#)]
4. Li, Y.; Zhang, J.; Li, H.; Fan, Y.; He, T.; Qiu, H.; Yin, S. Metallacycle/Metallacage-Cored Fluorescent Supramolecular Assemblies with Aggregation-Induced Emission Properties. *Adv. Optical Mater.* **2020**, *8*, 1902190. [[CrossRef](#)]
5. Li, B.; He, T.; Fan, Y.; Yuan, X.; Qiu, H.; Yin, S. Recent developments in the construction of metallacycle/metallacage-cored supramolecular polymers via hierarchical self-assembly. *Chem. Commun.* **2019**, *55*, 8036–8059. [[CrossRef](#)]
6. Xu, L.; Shen, X.; Zhou, Z.; He, T.; Zhang, J.; Qiu, H.; Saha, M.L.; Yin, S.; Stang, P.J. Metallacycle-Cored Supramolecular Polymers: Fluorescence Tuning by Variation of Substituents. *J. Am. Chem. Soc.* **2018**, *140*, 16920–16924. [[CrossRef](#)]
7. Chen, F.; Lin, X.; Li, Y.; Xu, D.; Qiu, H.; Yin, S. Metallacycle-crosslinked supramolecular polymers constructed by amino–YNE click reaction with enhanced mechanical properties. *Supramol. Mater.* **2022**, *1*, 100003. [[CrossRef](#)]
8. Zhang, Y.-Y.; Chen, F.; Li, Y.; Qiu, H.-Y.; Zhang, J.-J.; Yin, S.-C. Supramolecular Polymer Networks with Enhanced Mechanical Properties: The Marriage of Covalent Polymer and Metallacycle. *Chin. J. Chem.* **2021**, *39*, 2731–2737. [[CrossRef](#)]
9. Zhang, Q.; Tang, D.; Zhang, J.; Ni, R.; Xu, L.; He, T.; Lin, X.; Li, X.; Qiu, H.; Yin, S.; et al. Self-Healing Heterometallic Supramolecular Polymers Constructed by Hierarchical Assembly of Triply Orthogonal Interactions with Tunable Photophysical Properties. *J. Am. Chem. Soc.* **2019**, *141*, 17909–17917. [[CrossRef](#)]
10. Hu, Y.X.; Hao, X.T.; Xu, L.; Xie, X.; Xiong, B.; Hu, Z.; Sun, H.; Yin, G.-Q.; Li, X.; Peng, H.; et al. Construction of supramolecular liquid-crystalline metallacycles for holographic storage of colored images. *J. Am. Chem. Soc.* **2020**, *142*, 6285–6294. [[CrossRef](#)]
11. Chen, L.; Chen, C.L.; Sun, Y.; Lu, S.; Huo, H.; Tan, T.; Li, A.; Li, X.; Ungar, G.; Liu, F.; et al. Luminescent metallacycle-cored liquid crystals induced by metal coordination. *Angew. Chem. Int. Ed.* **2020**, *59*, 10143–10150. [[CrossRef](#)] [[PubMed](#)]
12. Zhang, M.; Yin, S.; Zhang, J.; Zhou, Z.; Saha Manik, L.; Lu, C.; Stang Peter, J. Metallacycle-cored supramolecular assemblies with tunable fluorescence including white-light emission. *Proc. Natl. Acad. Sci. USA* **2017**, *114*, 3044–3049. [[CrossRef](#)] [[PubMed](#)]
13. Zhang, M.; Saha, M.L.; Wang, M.; Zhou, Z.; Song, B.; Lu, C.; Yan, X.; Li, X.; Huang, F.; Yin, S.; et al. Multicomponent platinum(II) cages with tunable emission and amino acid sensing. *J. Am. Chem. Soc.* **2017**, *139*, 5067–5074. [[CrossRef](#)]
14. Saha, M.L.; Yan, X.Z.; Stang, P.J. Photophysical properties of organoplatinum(II) compounds and derived self-assembled metallacycles and metallacages: Fluorescence and its applications. *Acc. Chem. Res.* **2016**, *49*, 2527–2539. [[CrossRef](#)]
15. Xu, L.; Wang, Y.X.; Chen, L.J.; Yang, H.B. Construction of multiferrocenyl metallacycles and metallacages via coordination-driven self-assembly: From structure to functions. *Chem. Soc. Rev.* **2020**, *49*, 3889–3919.
16. Hong, T.; Zhang, Z.B.; Sun, Y.; Tao, J.-J.; Tang, J.-D.; Xie, C.; Wang, M.; Chen, F.; Xie, S.-S.; Li, S.; et al. Chiral metallacycles as catalysts for asymmetric conjugate addition of styrylboronic acids to α,β -Enones. *J. Am. Chem. Soc.* **2020**, *142*, 10244–10249. [[CrossRef](#)]
17. Kaphan David, M.; Levin Mark, D.; Bergman Robert, G.; Raymond Kenneth, N.; Toste, F.D. A supramolecular microenvironment strategy for transition metal catalysis. *Science* **2015**, *350*, 1235–1238. [[CrossRef](#)]
18. Zhu, H.; Li, Q.; Shi, B.; Ge, F.; Liu, Y.; Mao, Z.; Zhu, H.; Wang, S.; Yu, G.; Huang, F.; et al. Dual-Emissive Platinum(II) Metallacage with a Sensitive Oxygen Response for Imaging of Hypoxia and Imaging-Guided Chemotherapy. *Angew. Chem. Int. Ed.* **2020**, *59*, 20208–20214. [[CrossRef](#)]
19. Fan, Y.; Zhang, J.; Li, Y.; Chen, Q.; Ni, Z.; Zhou, H.; Yu, J.; Qiu, H.; Yin, S. Amphiphilic rhomboidal metallacycles with aggregation-induced emission and aggregation-caused quenching luminogens for white-light emission and bioimaging. *Mater. Chem. Front.* **2022**, *6*, 633–643. [[CrossRef](#)]
20. Yu, G.C.; Zhang, M.M.; Saha, M.L.; Mao, Z.; Chen, J.; Yao, Y.; Zhou, Z.; Liu, Y.; Gao, C.; Huang, F.; et al. Antitumor activity of a unique polymer that incorporates a fluorescent self-assembled metallacycle. *J. Am. Chem. Soc.* **2017**, *139*, 15940–15949. [[CrossRef](#)]
21. Zhou, Z.X.; Liu, J.P.; Rees, T.W.; Wang, H.; Li, X.; Chao, H.; Stang, P.J. Heterometallic Ru–Pt metallacycle for two-photon photodynamic therapy. *Proc. Natl. Acad. Sci. USA* **2018**, *115*, 5664. [[CrossRef](#)] [[PubMed](#)]

22. Gupta, G.; Sun, Y.; Das, A.; Stang, P.J.; Yeon Lee, C. BODIPY based metal-organic macrocycles and frameworks: Recent therapeutic developments. *Coord. Chem. Rev.* **2022**, *452*, 214308. [[CrossRef](#)] [[PubMed](#)]
23. Xu, Y.; Li, C.; Lu, S.; Wang, Z.; Liu, S.; Yu, X.; Li, X.; Sun, Y. Construction of emissive ruthenium(II) metallacycle over 1000 nm wavelength for in vivo biomedical applications. *Nat. Commun.* **2022**, *13*, 2009. [[CrossRef](#)] [[PubMed](#)]
24. Ding, Y.; Tong, Z.; Jin, L.; Ye, B.; Zhou, J.; Sun, Z.; Yang, H.; Hong, L.; Huang, F.; Wang, W.; et al. An NIR Discrete Metallacycle Constructed from Perylene Bisimide and Tetraphenylethylene Fluorophores for Imaging-Guided Cancer Radio-Chemotherapy. *Adv. Mater.* **2022**, *34*, 2106388. [[CrossRef](#)] [[PubMed](#)]
25. Lu, H.; Mack, J.; Yang, Y.C.; Shen, Z. Structural modification strategies for the rational design of red/NIR region BODIPYs. *Chem. Soc. Rev.* **2014**, *43*, 4778–4823. [[CrossRef](#)]
26. Sun, W.; Zhao, X.; Fan, J.; Du, J.; Peng, X. Boron Dipyrromethene Nano-Photosensitizers for Anticancer Phototherapies. *Small* **2019**, *15*, 1804927. [[CrossRef](#)]
27. Liu, M.; Ma, S.; She, M.; Chen, J.; Wang, Z.; Liu, P.; Zhang, S.; Li, J. Structural modification of BODIPY: Improve its applicability. *Chin. Chem. Lett.* **2019**, *30*, 1815–1824. [[CrossRef](#)]
28. Bassan, E.; Gualandi, A.; Cozzi, P.G.; Ceroni, P. Design of BODIPY dyes as triplet photosensitizers: Electronic properties tailored for solar energy conversion, photoredox catalysis and photodynamic therapy. *Chem. Sci.* **2021**, *12*, 6607–6628. [[CrossRef](#)]
29. Ito, F.; Nagai, T.; Ono, Y.; Yamaguchi, K.; Furuta, H.; Nagamura, T. Photophysical properties of 2-picolinoylpyrrole boron complex in solutions. *Chem. Phys. Lett.* **2007**, *435*, 283–288. [[CrossRef](#)]
30. Loudet, A.; Burgess, K. BODIPY Dyes and Their Derivatives: Syntheses and Spectroscopic Properties. *Chem. Rev.* **2007**, *107*, 4891–4932. [[CrossRef](#)]
31. Squeo, B.M.; Gregoriou, V.G.; Avgeropoulos, A.; Baysec, S.; Allard, S.; Scherf, U.; Chochos, C.L. BODIPY-based polymeric dyes as emerging horizon materials for biological sensing and organic electronic applications. *Prog. Polym. Sci.* **2017**, *71*, 26–52. [[CrossRef](#)]
32. Klifout, H.; Stewart, A.; Elkhalfi, M.; He, H. BODIPYs for dye-sensitized solar cells. *ACS Appl. Mater. Interfaces* **2017**, *9*, 39873–39889. [[CrossRef](#)]
33. Ma, X.; Azeem, E.A.; Liu, X.L.; Cheng, Y.; Zhu, C. Synthesis and tunable chiroptical properties of chiral BODIPY-based D- π -A conjugated polymers. *J. Mater. Chem. C* **2014**, *2*, 1076–1084. [[CrossRef](#)]
34. Bucher, L.; Desbois, N.; Harvey, P.D.; Sharma, G.D.; Gros, C.P. Porphyrins and BODIPY as Building Blocks for Efficient Donor Materials in Bulk Heterojunction Solar Cells. *Solar RRL* **2017**, *1*, 1700127. [[CrossRef](#)]
35. Miao, J.; Wang, Y.; Liu, J.; Wang, L. Organoboron molecules and polymers for organic solar cell applications. *Chem. Soc. Rev.* **2022**, *51*, 153–187. [[CrossRef](#)] [[PubMed](#)]
36. Li, S.; Liu, K.; Kuang, G.; Masuda, T.; Zhang, A. Thermoresponsive Helical Poly(phenylacetylene)s. *Macromolecules* **2014**, *47*, 3288–3296. [[CrossRef](#)]
37. Boens, N.; Leen, V.; Dehaen, W. Fluorescent indicators based on BODIPY. *Chem. Soc. Rev.* **2012**, *41*, 1130–1172. [[CrossRef](#)]
38. Nguyen, V.-N.; Ha, J.; Cho, M.; Li, H.; Swamy, K.M.K.; Yoon, J. Recent developments of BODIPY-based colorimetric and fluorescent probes for the detection of reactive oxygen/nitrogen species and cancer diagnosis. *Coord. Chem. Rev.* **2021**, *439*, 213936. [[CrossRef](#)]
39. Zhang, J.; Wang, N.; Ji, X.; Tao, Y.; Wang, J.; Zhao, W. BODIPY-Based Fluorescent Probes for Biothiols. *Chem. Eur. J.* **2020**, *26*, 4172–4192. [[CrossRef](#)]
40. Zhang, Y.F.; Bo, S.W.; Feng, T.; Qin, X.; Wan, Y.; Jiang, S.; Li, C.; Lin, J.; Wang, T.; Zhou, X.; et al. A versatile theranostic nanoemulsion for architecture-dependent multimodal imaging and dually augmented photodynamic therapy. *Adv. Mater.* **2019**, *31*, 1806444. [[CrossRef](#)]
41. Chen, X.; Liu, Y.C.; Cui, J.J.; Wu, F.Y.; Xiao, Q. A galactosidase-activatable fluorescent probe for detection of bacteria based on BODIPY. *Molecules* **2021**, *26*, 6072. [[CrossRef](#)] [[PubMed](#)]
42. Ni, Y.; Kannadorai, R.K.; Yu, S.W.K.; Chang, Y.-T.; Wu, J. Push-pull type meso-ester substituted BODIPY near-infrared dyes as contrast agents for photoacoustic imaging. *Org. Biomol. Chem.* **2017**, *15*, 4531–4535. [[CrossRef](#)] [[PubMed](#)]
43. Caruso, E.; Malacarne, M.C.; Marras, E.; Papa, E.; Bertato, L.; Banfi, S.; Gariboldi, M.B. New BODIPYs for photodynamic therapy (PDT): Synthesis and activity on human cancer cell lines. *Biorg. Med. Chem.* **2020**, *28*, 115737. [[CrossRef](#)] [[PubMed](#)]
44. Zhang, T.; Ma, C.; Sun, T.T.; Xie, Z. Unadulterated BODIPY nanoparticles for biomedical applications. *Coord. Chem. Rev.* **2019**, *390*, 76–85. [[CrossRef](#)]
45. Wang, Z.; Huang, L.; Yan, Y.; El-Zohry, A.M.; Toffoletti, A.; Zhao, J.; Barbon, A.; Dick, B.; Mohammed, O.F.; Han, G. Elucidation of the Intersystem Crossing Mechanism in a Helical BODIPY for Low-Dose Photodynamic Therapy. *Angew. Chem. Int. Ed.* **2020**, *59*, 16114–16121. [[CrossRef](#)]
46. Yogo, T.; Urano, Y.; Ishitsuka, Y.; Maniwa, F.; Nagano, T. Highly Efficient and Photostable Photosensitizer Based on BODIPY Chromophore. *J. Am. Chem. Soc.* **2005**, *127*, 12162–12163. [[CrossRef](#)]
47. Xi, D.M.; Xiao, M.; Cao, J.F.; Zhao, L.; Xu, N.; Long, S.; Fan, J.; Shao, K.; Sun, W.; Yan, X.; et al. NIR light-driving barrier-free group rotation in nanoparticles with an 88.3% photothermal conversion efficiency for photothermal therapy. *Adv. Mater.* **2020**, *32*, 1907855. [[CrossRef](#)]
48. Lin, Y.; Yin, J.; Li, X.; Pan, C.; Kuang, G. Luminescent BODIPY-based Porous Organic Polymer for CO₂ Adsorption. *J. Wunan Univ. Technol.* **2019**, *34*, 440–445. [[CrossRef](#)]

49. Su, M.; Han, Q.; Yan, X.; Liu, Y.; Luo, P.; Zhai, W.; Zhang, Q.; Li, L.; Li, C. A Supramolecular Strategy to Engineering a Non-photobleaching and Near-Infrared Absorbing Nano-J-Aggregate for Efficient Photothermal Therapy. *ACS Nano* **2021**, *15*, 5032–5042. [[CrossRef](#)]
50. Wang, X.; Lin, W.; Zhang, W.; Li, C.; Sun, T.; Chen, G.; Xie, Z. Amphiphilic redox-sensitive NIR BODIPY nanoparticles for dual-mode imaging and photothermal therapy. *J. Colloid Interface Sci.* **2019**, *536*, 208–214. [[CrossRef](#)]
51. Li, G.; Zhang, X.; Zhao, W.; Zhao, W.; Li, F.; Xiao, K.; Yu, Q.; Liu, S.; Zhao, Q. Stable and Well-Organized Near-Infrared Platinum(II)-Acetylide-Based Metallacycles-Mediated Cancer Phototherapy. *ACS Appl. Mater. Interfaces* **2020**, *12*, 20180–20190. [[CrossRef](#)] [[PubMed](#)]
52. Gupta, G.; Das, A.; Ghate, N.B.; Kim, T.; Ryu, J.Y.; Lee, J.; Mandal, N.; Lee, C.Y. Novel BODIPY-based Ru(ii) and Ir(iii) metallarectangles: Cellular localization of compounds and their antiproliferative activities. *Chem. Commun.* **2016**, *52*, 4274–4277. [[CrossRef](#)] [[PubMed](#)]
53. Gupta, G.; You, Y.; Hadiputra, R.; Jung, J.; Kang, D.-K.; Lee, C.Y. Heterometallic BODIPY-Based Molecular Squares Obtained by Self-Assembly: Synthesis and Biological Activities. *ACS Omega* **2019**, *4*, 13200–13208. [[CrossRef](#)]
54. Zhou, J.; Zhang, Y.Z.; Yu, G.C.; Crawley, M.R.; Fulong, C.R.P.; Friedman, A.E.; Sengupta, S.; Sun, J.; Li, Q.; Huang, F.; et al. Highly emissive self-assembled BODIPY-platinum supramolecular triangles. *J. Am. Chem. Soc.* **2018**, *140*, 7730–7736. [[CrossRef](#)]
55. Fang, J.; Islam, W.; Maeda, H. Exploiting the dynamics of the EPR effect and strategies to improve the therapeutic effects of nanomedicines by using EPR effect enhancers. *Adv. Drug Deliv. Rev.* **2020**, *157*, 142–160. [[CrossRef](#)] [[PubMed](#)]
56. Li, Y.; Yuan, X.C.; Yu, J.L.; Fan, Y.; He, T.; Lu, S.; Li, X.; Qiu, H.; Yin, S. Amphiphilic rhomboidal organoplatinum(II) metallacycles with encapsulated doxorubicin for synergistic cancer therapy. *ACS Appl. Bio Mater.* **2020**, *3*, 8061–8068. [[CrossRef](#)] [[PubMed](#)]
57. Sun, W.; Chen, R.; Cheng, X.J.; Marin, L. Bodipy-based chemosensors for highly sensitive and selective detection of Hg²⁺ ions. *New J. Chem.* **2018**, *42*, 19224–19231. [[CrossRef](#)]